

## Flow-accelerated corrosion behavior of 13Cr stainless steel in a wet gas environment containing CO<sub>2</sub>

Yong Li<sup>1)</sup>, Min-dong Chen<sup>1)</sup>, Jian-kuan Li<sup>1)</sup>, Long-fei Song<sup>1)</sup>, Xin Zhang<sup>2)</sup>, and Zhi-yong Liu<sup>1)</sup>

1) Corrosion and Protection Centre, Key Laboratory for Corrosion and Protection (MOE) National Environmental Corrosion Platform (NECP), University of Science and Technology Beijing, Beijing 100083, China

2) Nuclear and Radiation Safety Center, Ministry of Environmental Protection of P.R. China, Beijing 100082, China

(Received: 22 November 2017; revised: 10 April 2018; accepted: 13 April 2018)

**Abstract:** This work investigated the flow-accelerated corrosion (FAC) behavior of 13Cr in a wet CO<sub>2</sub>-containing environment at different flowing gas velocities and impinging angles, with the natural-gas pipeline environment simulated by a self-assembled impingement jet system. Surface morphology determination, electrochemical measurements, and hydromechanics numerical analysis were carried out to study the FAC behavior. The results demonstrate that pitting corrosion was the primary mode of corrosion in 13Cr stainless steel. High-flow-rate gas destroyed the passive film and decreased the pitting potential, resulting in more serious corrosion. The corrosion degree with various impact angles showed the following order: 90° > 60° > 45°. The shear force and the electrolyte from the flowing gas were concluded to be the determinant factors of FAC, whereas the shear force was the main factor responsible for destroying the passive film.

**Keywords:** flow-accelerated corrosion; jet loop; flowing velocity; impact angle; CO<sub>2</sub>

### 1. Introduction

Corrosion in the natural-gas transportation infrastructure often results in security accidents [1]. H<sub>2</sub>S, CO<sub>2</sub>, and other corrosive agents in natural gas dissolved in H<sub>2</sub>O are corrosive to the pipeline steel [2]. Because of the normal shortage of deep dehydration of natural gas in real environments, water vapor can condense to an electrolyte film containing corrosive agents on the pipeline walls when the humidity levels reach saturation, leading to corrosion [3–4]. Some studies have shown that the humidity of the natural gas affects the corrosion of pipeline steel [5–7]. Furthermore, fluids with a high flow velocity, especially fluids containing CO<sub>2</sub>, have been demonstrated to accelerate corrosion [8–10]. Thus, corrosion resulting from flowing gas containing CO<sub>2</sub> in wet environments should be given more attention.

Flow-accelerated corrosion (FAC) occurs in a corrosive environment in which the flowing gas accelerates the corrosion rate; specifically, the common effect of the electrochemical action and mechanical factor from the fluid increases the corrosion rate [11–13]. FAC has been reported to

strongly influence the corrosion and to be the main factor responsible for the failure of the pipeline material [14]. Many authors have reported that damage to the protective film and the metal surface from the fluid can cause more serious corrosion [15–16], especially when the fluid contains solid particles or corrosion products [17–18]. In addition, FAC has been speculated to result from the interaction between electrochemical action and damage to the protective film resulting from the shear force of the fluid [8]. Thus, FAC should be investigated more intensively, especially in natural-gas environments, because only a few studies on gas environments have been reported and because the differences between flowing gas environments and liquid/solid or multiphase environments are substantial. Notably, an actual pipeline will suffer severe barometric surges from different scouring angles at bends associated with the use of special components such as elbow and tee joints, resulting in a change in the shear stress [19]. Most gas pipeline failures occur in these areas; however, research on this aspect is scarce. Therefore, FAC behavior and the effects of scouring angles on this behavior in natural-gas environments warrant

Corresponding author: Zhi-yong Liu E-mail: liuzhiyong7804@126.com

© University of Science and Technology Beijing and Springer-Verlag GmbH Germany, part of Springer Nature 2018

further investigation.

Generally, three methods are used to study FAC: loop systems [20], impingement jet systems [21], and the rotating-disc electrode (RDE) or the rotating-cylinder electrode (RCE) method [22]. However, loop systems and RDE/RCE are suitable only in liquid-dominated environments and cannot be used in natural-gas environments. The process in which the natural gas scours the surface can be simulated with an impingement jet system. Therefore, FAC behavior can be investigated by simulating actual natural gas transport with an impingement jet system [23–24].

To meet the challenges in the exploitation of natural gas, stainless steels have been used in mechanical engineering efforts. 13Cr stainless steel can be used in a wide range of applications because of its good ductility, machinability, weldability, and especially good corrosion resistance. The passive film of 13Cr stainless steel, consisting of  $\text{FeCO}_3$ ,  $\text{Cr}(\text{OH})_3$ , and  $\text{Cr}_2\text{O}_3$ , is considered to exhibit strong protective characteristics in environments containing  $\text{CO}_2$  [25–26]. Thus, studying the FAC behavior of 13Cr stainless steel in simulated natural-gas environments is vital for the steel's use in mechanical engineering.

In the present work, a self-assembled impingement jet system was used to simulate the natural gas with different flowing velocities and impinging angles. The effect of flowing velocity and impact angle on the FAC behavior of 13Cr in a gas environment containing  $\text{CO}_2$  was investigated by hydromechanical numerical analysis, corrosion morphology analysis, and electrochemical measurements. Such research provides essential insights into the FAC

behavior of 13Cr stainless steel in an actual gas pipeline environment.

## 2. Experimental

### 2.1. Material and environment

The experimental material used in this work was 13Cr stainless steel with a chemical composition (wt%) of 0.18 C, 0.85 Si, 0.18 Ni, 13.1 Cr, 0.95 Mn, 0.01 S, 0.17 Cu, and 0.02 P, with the balance comprising Fe.

The actual natural gas transportation environment was simulated in a flow-accelerated corrosion apparatus with 80% relative humidity, atmospheric pressure,  $\text{N}_2$  as a noncorrosive gas, a  $\text{N}_2/\text{CO}_2$  ratio of 9:1, and a temperature  $(25 \pm 1)^\circ\text{C}$ . The gas flow rate, humidity, and ratio were controlled by adjusting valves, as shown in Fig. 1. A flow meter was installed between the outlet in Fig. 1(a) and the inlet in Fig. 1(b) to calculate the gas flow ( $L$ ). Fig. 1(a) shows the natural gas simulation device, in which the ratio of  $\text{N}_2/\text{CO}_2$  was controlled via adjusting valves V1 and V2 according to the values of pressure gauges P1 and P2, respectively. The wet gas was achieved by passing the dry gas through vapor to achieve a certain humidity level in the gas, as indicated by the humidity sensor, the value of which was controlled via adjusting valves V3, V4, and V5 according to the values of pressure gauges P3 and P4. The distance and impinging angle between the nozzle and the surface of the sample were altered via adjustment of the position fixed on the sample holder, where the nozzle-to-sample distance was 2 mm and the nozzle diameter ( $d$ ) was 1 mm.

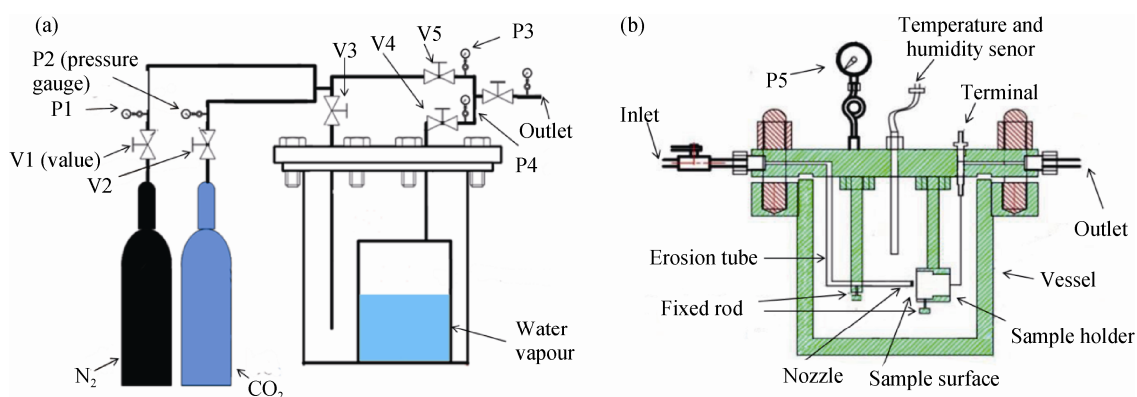


Fig. 1. Schematic of the flow-accelerated corrosion apparatus: (a) natural gas simulation; (b) scouring apparatus.

The flowing gas velocity from the nozzle was calculated by

$$v_a = \frac{4L}{\pi d^2} \quad (1)$$

where  $v_a$  is the flow velocity from the nozzle. However, the

actual flow velocity scouring on the surface of the sample was smaller than the  $v_a$  value calculated by Eq. (1) because of the distance between the nozzle and the surface, as shown in Fig. 2. The actual flow velocity impinging on the sample was calculated by the software FloEFD 12.1, and the results

are shown in Table 1. The impacting angles in the study were 45°, 60°, and 90°.

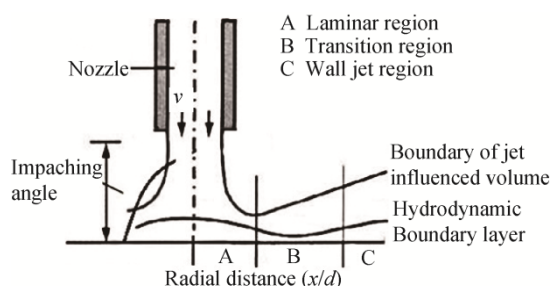


**Fig. 2.** Simulation of fluid mechanics in the injection scouring model.

**Table 1.** Actual scouring velocities according to the initial flow velocities

Initial flow velocity / (m·s <sup>-1</sup> )	Actual flow velocity / (m·s <sup>-1</sup> )
10	2
15	6
30	14
50	28

## 2.2. Electrochemical test

The dual-electrode model was used for electrochemical

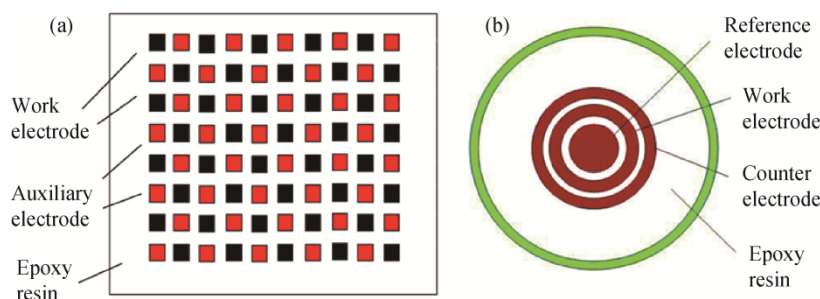


**Fig. 3.** Samples for the electrochemical tests: (a) EIS; (b) polarization curves.

All of the samples were polished to 5000 grit with fine-grain emery paper and then cleaned with acetone. The Ag/AgCl electrode was checked by referring to a standard hydrogen electrode in 1 mol/L KCl solution; the corresponding reference electrode potential was 0.25 V and changed by 0.5 mV over 12 h, which completely conformed to the requirements for a reference electrode. After 2 h of scouring, all tests were carried out on a Gamry Reference 3000 electrochemical workstation. After the open-circuit potential (OCP) stabilized, EIS was carried out in the frequency range from 100 kHz to 10 mHz, with a sinusoidal disturbance signal of 10 mV at OCP. The polarization curves were recorded at a scanning rate 0.5 mV/s over the scanning range from -0.5 V to 1.2 V vs. OCP.

impedance spectroscopy (EIS); the auxiliary and working electrodes (titanium alloy and 13Cr steel) were arranged in alternating fashion, as shown in Fig. 3. The dimensions of all of the electrodes used in the EIS experiments were 1 mm × 1 mm × 3 mm, and copper wires were soldered onto their back surfaces. The electrodes were coated with epoxy resin, leaving a work area of 1 mm × 1 mm, with a distance of 0.5 mm. In the tests, the electrodes were placed parallel to each other and were insulated from their neighboring electrodes.

The polarization curves were recorded with a concentric three-electrode system. Fig. 3(b) shows the sample, with an Ag/AgCl electrode as the reference electrode, the 13Cr steel sample as the working electrode, and a titanium alloy electrode as the auxiliary electrode. The samples were coated with epoxy and soldered with copper wires at their back. The diameter of the reference electrode was 1.5 mm, the inner and outer diameters of the working electrode were 2 mm and 3 mm, respectively, and the inner and outer diameters of the auxiliary electrode were 4 mm and 5 mm, respectively. The electrodes were positioned in an alternating arrangement and were insulated from their neighbors, as shown in Fig. 3(b).

## 2.3. Surface morphology

Samples with dimensions of 15 mm × 15 mm × 3 mm were embedded in phenolic molding powder, leaving a working surface 15 mm × 15 mm, for observation of their surface morphology. The samples were polished from 60 to 5000 grit with fine-grained emery paper and were then cleaned with acetone and dried with a dryer. After being scoured for 12 h, the samples were withdrawn from the vessel, cleaned with acetone, and dried under a stream of nitrogen. The surface morphology of the samples was observed by optical microscopy and scanning electron microscopy (SEM; Cambridge S-360 SEM); the corrosion composition was analyzed by energy-dispersive spectrometry (EDS). After the samples were derusted at 60°C for 20 min

with a solution composed of 100 mL of HNO<sub>3</sub> and 1000 mL of distilled water, the samples were cleaned sequentially with distilled water and acetone and then dried in a dryer. The pit depth was analyzed according to the distance of the position from the center of the scouring point; the distribution and pitting depth were observed with a stereoscopic microscope (Keyence VHX-2000).

According to the mass transfer coefficients ( $K$ ) [27], the surface subjected to FAC was divided into three parts according to the value of  $x/d$  (where  $x$  is the distance of the position from the center of the scouring point): central area A ( $x/d < 1.1$ ), transitional area B ( $1.1 < x/d < 2.2$ ), and lateral area C ( $x/d > 2.2$ ), as shown in Fig. 2. The mass transfer coefficient at the central area ( $K_{\text{cen}}$ ) and the transitional area ( $K_{\text{tran}}$ ) are defined as [27]

$$K_{\text{cen}} = 0.76d^{-0.5}y^{-0.17}D^{0.67}v^{0.5}, \quad \frac{x}{d} \leq 1.1 \quad (2)$$

$$K_{\text{tran}} = 1.04d^{-0.5}y^{-0.17}D^{0.67}v^{0.5}, \quad \frac{x}{d} \leq 2.2 \quad (3)$$

where  $y$  is the kinematic viscosity,  $v$  is the flow velocity and  $D$  is the diffusion coefficient.

All the tests were carefully conducted in triplicate to en-

sure the reproducibility and reliability of the results.

### 3. Results

#### 3.1. Effect of flow velocity

Fig. 4 shows the microscopic microstructure of the central area of the sample after FAC for 12 h at an impact angle of 90° under various flow velocities. The number and radius of pits increased with increasing flow velocity. The most severe corrosion occurred at the flow velocity of 28 m/s, as judged by the number of pits. When the flow velocity increased from 2 m/s to 14 m/s, the increase in FAC was small; we concluded that 28 m/s was the critical velocity for the 80% humidity condition.

Fig. 5 shows the Nyquist plots for 13Cr stainless steel in the central area at an impact angle of 90° with different flow velocities. As shown in Fig. 5(a), only a capacitive loop can be observed. The arc radius with the flow velocity of 2 m/s was the biggest. Increasing the flow velocity decreased the radius, indicating that corrosion resistance decreased with increasing flow velocity. Fig. 5(b) shows the corresponding Bode diagram. The phase angle was higher than 45° at low frequencies, and a break occurred at high frequencies.

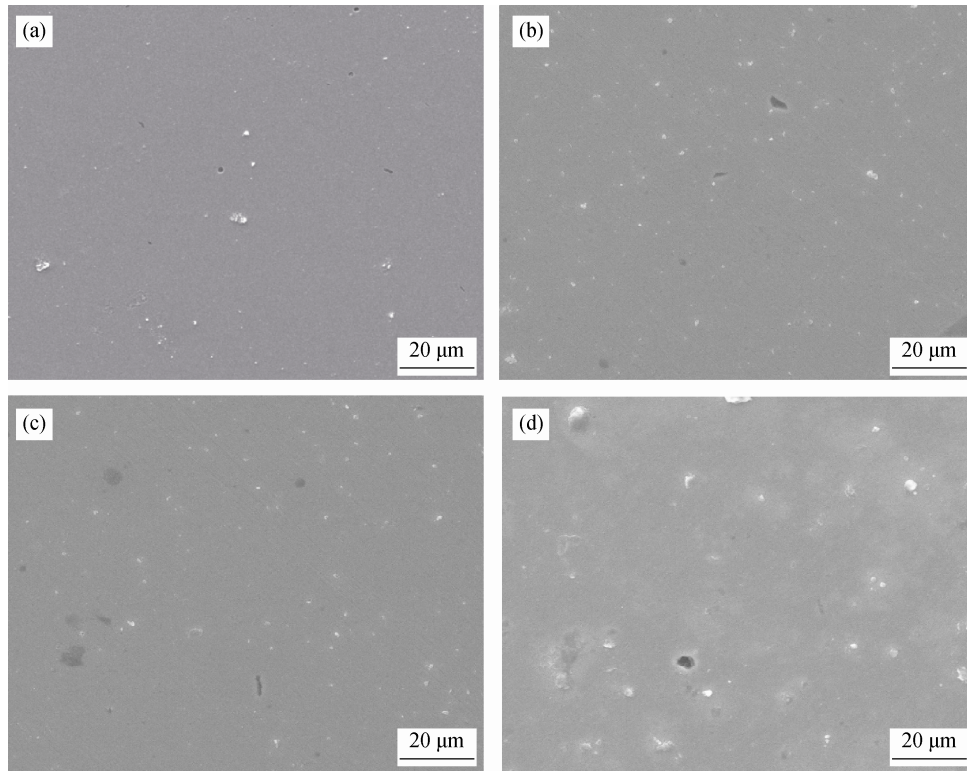


Fig. 4. SEM surface morphologies in the central area of 13Cr stainless steel samples under flow velocities of 2 m/s (a), 6 m/s (b), 14 m/s (c), and 28 m/s (d) at an impinging angle of 90°.

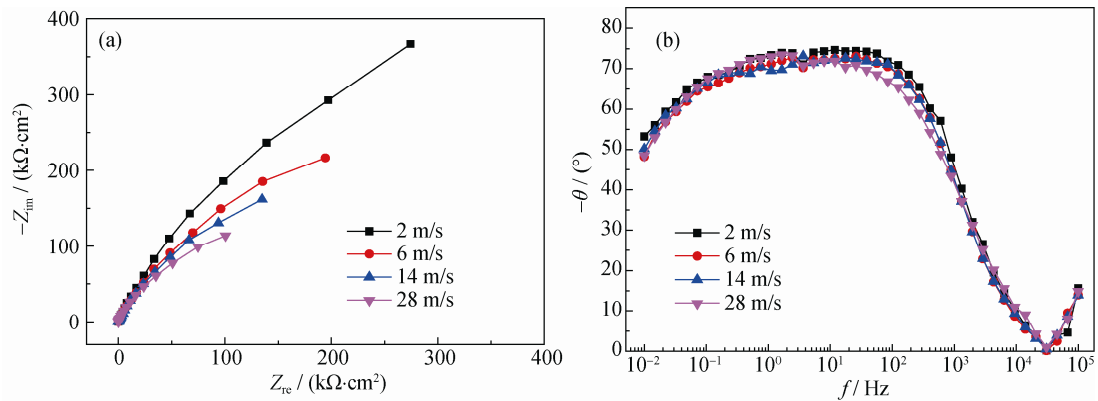


Fig. 5. Nyquist (a) and Bode plots (b) of 13Cr stainless steel at different flow velocities with an impinging angle of 90°.

The impedance data in Fig. 5 were fitted using the ZsimpWin software; the equivalent circuit is shown in Fig. 6, and the results are shown in Table 2. In Fig. 6,  $R_s$  is the solution resistance,  $Q_f$  is the capacitance of the corrosion film,  $R_f$  represents the resistance of the corrosion film,  $Q_{dl}$  is the charge transfer capacitance of the electric double layer, and  $R_{dl}$  is the charge transfer resistance of the electric double layer. Table 2 shows that  $R_s$  and  $R_f$  decreased with increasing flow velocity and that the values corresponding to flow velocity of 28 m/s were the smallest. These results indicate that high flow velocity enhanced the transport of the

electrolyte and destroyed the passive film. The value of resistance was mainly controlled by  $R_{dl}$ ; the variation is shown in Fig. 7. The value of  $R_{dl}$  decreased with increasing flow velocity, indicating that high flow velocity increased the transfer resistance of the electric double layer.

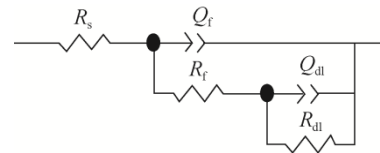


Fig. 6. Equivalent circuit used to model the EIS data.

Table 2. The fitting results

Flow velocity / (m·s <sup>-1</sup> )	$R_s / (\Omega\cdot\text{cm}^2)$	$Q_f / (\text{F}\cdot\text{cm}^{-2}\cdot\text{Hz}^{1-n})$	$n_1$	$R_f / (\Omega\cdot\text{cm}^2)$	$Q_{dl} / (\text{F}\cdot\text{cm}^{-2}\cdot\text{Hz}^{1-n})$	$n_2$	$R_{dl} / (\Omega\cdot\text{cm}^2)$
2	34.15	$1.010 \times 10^{-5}$	0.6978	16.029	$5.276 \times 10^{-6}$	0.9166	$1.782 \times 10^6$
6	26.39	$1.721 \times 10^{-5}$	0.8596	17.93	$7.185 \times 10^{-6}$	0.6291	$7.798 \times 10^5$
14	14.32	$1.482 \times 10^{-5}$	0.6512	15.51	$1.861 \times 10^{-5}$	0.8765	$6.909 \times 10^5$
28	2.638	$1.881 \times 10^{-8}$	0.7925	13.23	$4.816 \times 10^{-5}$	0.8137	$3.323 \times 10^5$

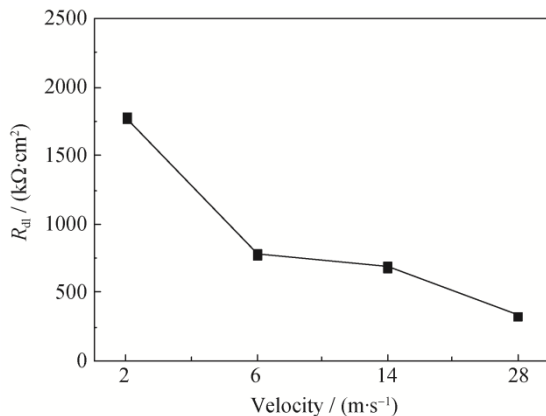


Fig. 7. The charge transfer resistance as a function of flow velocity.

Fig. 8 shows the polarization curves of 13Cr stainless steel impacted at 90° with different flow velocities. Changes in the corrosion potential and current with increasing flow

velocity were not obvious. The pitting potential (determined by the intersection of the tangent lines of current density in the passive range and the breakdown stage) at a flow of 2 m/s was the highest, and the pitting potential at a flow velocity of 28 m/s was the lowest. The high flow velocity obviously decreased the pitting potential. The results are consistent with the results in Figs. 4 and 5. We concluded that a high flow velocity destroyed the passive film, accelerating the pitting corrosion.

### 3.2. Corrosion analysis and evaluation

Fig. 9 shows the statistics of pit depth after derusting at various locations according to the distance from the center of the scouring point on the surface of samples scoured at different flow velocities and at an impinging angle of 90°. As shown in the figure, the deepest pits were observed for the flow velocity of 28 m/s; pit corrosion with the flow

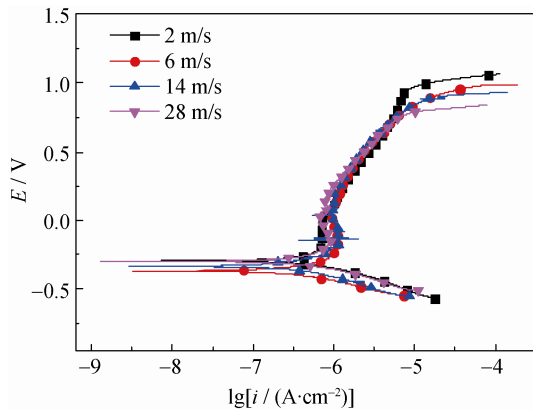


Fig. 8. Polarization curve for 13Cr stainless steel scoured at different flow velocities and at an impinging angle of 90°.

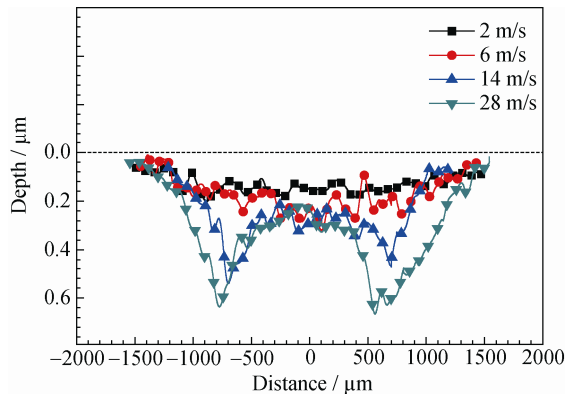


Fig. 9. Statistics of pit depth at various locations on the surface at different flow velocities with an impinging angle of 90°.

velocity of 2 m/s was weak, and high flow velocity increased the pit depth. The most serious pit corrosion occurred at the transportation area (distance 500  $\mu\text{m}$  to 1500  $\mu\text{m}$  from the center) with the flow velocities of 14 m/s and 28 m/s. The corrosion of the lateral area (distance greater than 1500  $\mu\text{m}$  from the center) was weak, whereas that of the center area (distance smaller than 1500  $\mu\text{m}$ ) was moderate. Hence, 14 m/s was the critical flow velocity of FAC for 13Cr stainless steel.

Fig. 10 shows the statistics of corrosion pit depth after derusting for FAC of 13Cr stainless steel at different impinging angles. Because the FAC of 13Cr stainless steel at low flow velocities was weak, the statistics of corrosion pit depth with the flow velocity of 28 m/s was conducted, as shown in Fig. 10. The greatest depth value of the corrosion pits was 0.66  $\mu\text{m}$ , 0.55  $\mu\text{m}$ , and 0.32  $\mu\text{m}$  at impinging angles of 90°, 60°, and 45°, respectively. The deepest pits were observed in the curve at an impinging angle of 90°. The location where the deepest pits occurred moved outward from the center with decreasing impinging angle. At impinging angles of 60° and 45°, the corrosion in the flow direction

was more serious than that on the other side. Overall, the corrosion degree with various impact angles showed the following order: 90° > 60° > 45°.

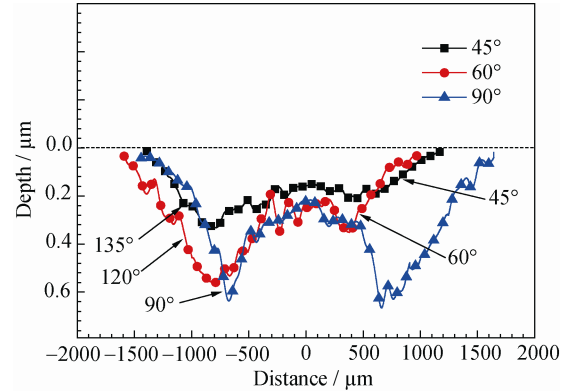


Fig. 10. Average corrosion rate at various locations on the surface, with a flow velocity of 28 m/s at different impinging angles.

## 4. Discussion

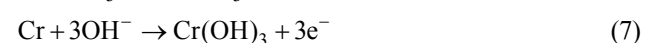
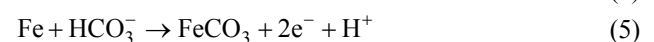
### 4.1. Effect of flow velocity on FAC

To investigate the reaction mechanism, we used EDS to analyze the corrosion products after FAC; the results are shown in Table 3. After Fe, C, and O, Cr was the dominant element in the corrosion products; the Cr concentration was greater than 13.1%, indicating that Cr was enriched in the corrosion products. These results demonstrate that the oxidative product of Cr generated in the electrochemical reaction and attached to the metal surface could protect metal from corrosion.

Table 3. Results of EDS analysis of the corrosion products under different flow velocities

Velocity / (m·s <sup>-1</sup> )	C	O	Fe	Cr
2	3.55	15.63	60.91	19.91
6	3.34	17.27	61.83	17.56
14	3.30	16.32	62.85	17.53
28	2.51	15.91	62.73	18.85

Cr can enhance the stain resistance of metals, especially in environments that contain CO<sub>2</sub> gas. The main corrosion mechanism of 13Cr is summarized as follows [25–26]:



Cr(OH)<sub>3</sub> would dehydrate to generate Cr<sub>2</sub>O<sub>3</sub> and other Cr compounds:



The corrosion products mainly consisted of FeCO<sub>3</sub> and Cr(OH)<sub>3</sub> when 13Cr stainless steel was scoured under the electrolyte with CO<sub>2</sub>. As shown in Fig. 4, most of the samples' surfaces were protected from corrosion, meaning that a compact passive film formed and protected the metallic matrix, which mainly consisted of Cr compounds.

FAC behavior was affected by the electrochemical reaction and by scouring. In the presence of H<sub>2</sub>O, the electrochemical reaction occurred on the surface of the metal while the flowing electrolyte accelerated the transport of the ions in the electrochemical reaction process, resulting in a high corrosion rate. As shown in Figs. 5 and 7, high flow velocity decreased the resistance of the 13Cr stainless steel, especially the charge transfer resistance of the electric double layer (Table 2). In contrast, the destruction of the passive film (Fig. 4) decreased the pitting potential (Fig. 8), which reduced the protection ability of the passive film and increased the corrosion rate. Furthermore, the shear force from the flowing gas damaged the protective film on the surface of the metal [11–12]; in addition, solid corrosion particles containing additional corrosion products, which led to high shear force, resulted in more serious damage to the film, which increased the corrosion rate, leading to more corrosion products. The shear force of the flowing gas was related to the flow velocity and size and density of the corrosion products.

As shown in Fig. 4, high gas flow rates led to the formation of more pits in the metal surface as a result of damage to the protective film. The damage of the passive film accelerated the reaction. The region where the passive film was damaged acted as an anode in the electrochemical reaction, the rate of which was higher than at the other regions, resulting in pits on the surface of the metal. Thus, we concluded that FAC of 13Cr stainless steel was caused by the combined effect of shear force and electrochemical reaction [13].

#### 4.2. Analysis of pit distribution

The shear stress resulting from the flowing gas was one of the main factors affecting the FAC. The distribution of the direction and velocity of the flowing gas on the surface of the metal was not uniform, which caused an asymmetric distribution of the pitting locations. As shown in Fig. 2, according to hydromechanics and the effect of the shear stress on the surface of the metal, the degree of corrosion on the surface was divided into three areas: laminar zone A (central area), transitional area B, and jet region C (lateral area). We speculate that the central area A experienced a low velocity and smaller shear stress; the effect of the flow gas on the

electrolyte process and the shear force was not obvious, and few pits were observed. The transitional area B suffered great shear force and electrochemical reaction, resulting in many pits, whereas lateral area C mainly suffered electrochemical reaction resulting from the gradual decrease in the shear force and mass transfer, as shown in Fig. 9.

The shear force from the flow gas on the surface of the metal can be divided into two components: the force in the normal direction and that in the tangential direction. The effect of the flow gas can be expressed by energy ( $E$ ) as

$$E = \frac{p^2}{2m} \quad (9)$$

where  $p$  is the fluid momentum,  $m$  is the fluid quality. In addition, the energy of the shear force in the normal direction ( $E_{\text{normal}}$ ) and that in the tangential direction ( $E_{\text{lateral}}$ ) can be expressed as

$$E_{\text{normal}} = \frac{(p \sin \phi)^2}{2m} = \frac{mv^2}{2} \sin^2 \phi \quad (10)$$

$$E_{\text{lateral}} = \frac{(p \cos \phi)^2}{2m} = \frac{mv^2}{2} \cos^2 \phi \quad (11)$$

where  $\phi$  is the eroding angle, and  $v$  is the flow velocity. Thus, with the impinging angle of 90°, the eroding angle was 0°, indicating that the central area suffered only the electrochemical reaction without the shear force parallel to the surface and that the outer area of the center suffered the shear stress. Thus, we concluded that the pit depth influenced by the flowing velocity in Fig. 10 was caused by the shear force and the impinging angle.

According to Refs. [28–30], the shear force can be defined as

$$\tau_p = \Delta P \frac{d}{4l} \quad (12)$$

where  $\tau_p$  is the shear force,  $l$  is the flow distance,  $d$  is the nozzle diameter, and  $\Delta P$  is the pressure drop over the flow distance. The  $\Delta P$  can be calculated by

$$\Delta P = f \cdot \frac{1}{d} \cdot \frac{\rho v^2}{2} \quad (13)$$

where  $v$  is the flow velocity,  $f$  is the D'Arcy friction coefficient of the flow, and  $\rho$  is the density of the fluid. Thus,

$$\tau_p = \frac{1}{8} \rho f v^2 \quad (14)$$

The  $f$  can be represented by the Reynolds number  $Re$  as

$$f = \frac{64}{Re} \quad (15)$$

where  $Re$  is defined as [31]

$$Re = \frac{dv}{\gamma} \quad (16)$$

where  $d$  is the diameter of the nozzle,  $v$  is the flow velocity,

and  $\gamma$  is the kinetic viscosity of the fluid. In this work,  $\gamma \approx 0.01 \text{ cm}^2 \cdot \text{s}^{-1}$ . Therefore, Eq. (12) can be represented by Eqs. (14)–(16) as

$$\tau_p = \frac{8\rho\gamma v}{d} \quad (17)$$

We therefore concluded that the shear force is proportional to the velocity; the shear force increases with increasing flowing velocity. Thus, the shear force determined by flowing velocity was the main factor responsible for severe pitting, as shown in Fig. 9.

## 5. Conclusions

In this study, the FAC behavior of 13Cr stainless steel was investigated at different gas flow velocities and impacting angles in a wet gas environment containing CO<sub>2</sub>. Pitting corrosion was observed, which accelerated with increasing flow rate of gas. The transition area obviously suffered the most serious pitting corrosion when the gas flow was greater than 14 m/s. With a decrease in the impact angle, the locations where the deepest pits occurred moved outward from the scouring center and the pitting degree decreased ( $90^\circ > 60^\circ > 45^\circ$ ).

The FAC behavior was controlled by the electrolyte diffusion rate and by the shear stress from the flowing gas. The shear force was the main factor responsible for destroying the passive film, thereby accelerating the corrosion rate.

## Acknowledgements

This study was supported by the National Environmental Corrosion Platform (NECP), the National Key Technology R&D Program of China (No. 2011BAK06B01-01-02) and the Fundamental Research Funds for the Central Universities of China (No. FRF-BR-17-028A).

## References

- [1] X.G. Li, D.W. Zhang, Z.Y. Liu, Z. Li, C.W. Du, and C.F. Dong, Materials science: share corrosion data, *Nature*, 527(2015), No. 7579, p. 441.
- [2] S. Nešić, Key issues related to modelling of internal corrosion of oil and gas pipelines—a review, *Corros. Sci.*, 49(2007), No. 12, p. 4308.
- [3] J.W. Yang, H<sub>2</sub>S/CO<sub>2</sub> corrosion of X60 pipeline steel in wet gas and solution, *Acta Metall. Sin.*, 44(2008), No. 11, p. 1366.
- [4] S.S. Rajahram, T.J. Harvey, and R.J.K. Wood, Erosion-corrosion resistance of engineering materials in various test conditions, *Wear*, 267(2009), No. 1-4, p. 244.
- [5] K. Najmi, B.S. McLaury, S.A. Shirazi, and S. Cremaschi, Experimental study of low concentration sand transport in wet gas flow regime in horizontal pipes, *J. Nat. Gas Sci. Eng.*, 24(2015), p. 80.
- [6] P.B. Machado, J.G.M. Monteiro, J.L. Medeiros, H.D. Epsom, and O.Q.F. Araujo, Supersonic separation in onshore natural gas dew point plant, *J. Nat. Gas Sci. Eng.*, 6(2012), p. 43.
- [7] L.T. Wang, Y.Y. Xing, Z.Y. Liu, D.W. Zhang, C.W. Du, and X.G. Li, Erosion-corrosion behavior of 2205 duplex stainless steel in wet gas environments, *J. Nat. Gas Sci. Eng.*, 35(2016), p. 928.
- [8] X.M. Hu and A. Neville, CO<sub>2</sub> erosion-corrosion of pipeline steel (API X65) in oil and gas conditions—a systematic approach, *Wear*, 267(2009), No. 11, p. 2027.
- [9] A. Kahyarian, M. Singer, and S. Nestic, Modeling of uniform CO<sub>2</sub> corrosion of mild steel in gas transportation systems: a review, *J. Nat. Gas Sci. Eng.*, 29(2016), p. 530.
- [10] M. Bagheri, A. Alamdari, and M. Davoudi, Quantitative risk assessment of sour gas transmission pipelines using CFD, *J. Nat. Gas Sci. Eng.*, 31(2016), p. 108.
- [11] L. Giourntas, T. Hodgkiess, and A.M. Galloway, Comparative study of erosion-corrosion performance on a range of stainless steels, *Wear*, 332-333(2015), p. 1051.
- [12] D.A. López, T. Pérez, and S.N. Simison, The influence of microstructure and chemical composition of carbon and low alloy steels in CO<sub>2</sub> corrosion. A state-of-the-art appraisal, *Mater. Des.*, 24(2003), No. 8, p. 561.
- [13] G.A. Zhang and Y.F. Cheng, Electrochemical corrosion of X65 pipe steel in oil/water emulsion, *Corros. Sci.*, 51(2009), No. 4, p. 901.
- [14] M.A. Islam and Z.N. Farhat, The synergistic effect between erosion and corrosion of API pipeline in CO<sub>2</sub> and saline medium, *Tribol. Int.*, 68(2013), p. 26.
- [15] R.J.K. Wood, J.C. Walker, T.J. Harvey, S. Wang, and S.S. Rajahram, Influence of microstructure on the erosion and erosion-corrosion characteristics of 316 stainless steel, *Wear*, 306(2013), No. 1-2, p. 254.
- [16] E. Mahdi, A. Rauf, and E.O. Eltai, Effect of temperature and erosion on pitting corrosion of X100 steel in aqueous silica slurries containing bicarbonate and chloride content, *Corros. Sci.*, 83(2014), p. 48.
- [17] Y.L. Zhao, F. Zhou, J. Yao, S.G. Dong, and N. Li, Erosion-corrosion behavior and corrosion resistance of AISI 316 stainless steel in flow jet impingement, *Wear*, 328-329(2015), p. 464.
- [18] G.A. Zhang, L.Y. Xu, and Y.F. Cheng, Investigation of erosion-corrosion of 3003 aluminum alloy in ethylene glycol-water solution by impingement jet system, *Corros. Sci.*, 51(2009), No. 2, p. 283.
- [19] W.M. Zhao, C. Wang, T.M. Zhang, M. Yang, B. Han, and A. Neville, Effects of laser surface melting on erosion-corrosion of X65 steel in liquid-solid jet impingement conditions, *Wear*, 362-363(2016), p. 39.
- [20] G.A. Zhang, L. Zeng, H.L. Huang, and X.P. Guo, A study of flow accelerated corrosion at elbow of carbon steel pipeline by array electrode and computational fluid dynamics simula-

- tion, *Corros. Sci.*, 77(2013), p. 334.
- [21] S. Papavinasam, R. Revie, M. Attard, A. Demoz, and K. Michaelian, Comparison of laboratory methodologies to evaluate corrosion inhibitors for oil and gas pipelines, *Corrosion*, 59(2003), No. 10, p. 897.
- [22] X. Jiang, Y.G. Zheng, and W. Ke, Effect of flow velocity and entrained sand on inhibition performances of two inhibitors for CO<sub>2</sub> corrosion of N80 steel in 3% NaCl solution, *Corros. Sci.*, 47(2005), No. 11, p. 2636.
- [23] A.H. Hosseinloo, F.F. Yap, and L.Y. Lim, Design and analysis of shock and random vibration isolation system for a discrete model of submerged jet impingement cooling system, *J. Vib. Control*, 21(2015), No. 3, p. 468.
- [24] H. Luo, C.F. Dong, X.G. Li, and K. Xiao, The electrochemical behaviour of 2205 duplex stainless steel in alkaline solutions with different pH in the presence of chloride, *Electrochim. Acta*, 64(2012), p. 211.
- [25] X.F. Wang, Z.J. Dong, Y.J. Liang, Z.H. Zhang, and C.F. Chen, Development of economic steels with low Cr content for anti-corrosion oil tube, *Corros. Sci. Protect. Technol.*, 18(2006), No. 6, p. 436.
- [26] H. Takabe and M. Ueda, The relationship between CO<sub>2</sub> corrosion resistance and corrosion products structure on carbon and low Cr bearing steels, *Corros. Eng.*, 56(2007), No. 11, p. 514.
- [27] G.A. Zhang and Y.F. Cheng, Electrochemical characterization and computational fluid dynamics simulation of flow-accelerated corrosion of X65 steel in a CO<sub>2</sub>-saturated oil-field formation water, *Corros. Sci.* 52(2010), No. 8, p. 2716.
- [28] K. Stewartson, *Mechanics of Fluids*, Nature, 272(1978), No. 5648, p. 109.
- [29] B.S. Massey and J. Ward-Smith, *Mechanics of Fluids*, CRC Press, Boca Raton, 1998, p. 36.
- [30] B.R. Munson, D.F. Young, and T.H. Okiishi, *Fundamentals of Fluid Mechanics*, 3rd Ed. Wiley, New York, 1990, p. 16.
- [31] M. Metikoš-Huković, I. Škugor, Z. Grubač, and R. Babić, Complexities of corrosion behaviour of copper-nickel alloys under liquid impingement conditions in saline water, *Electrochim. Acta*, 55(2010), No. 9, p. 3123.